Understanding the near-field photoacoustic spatiotemporal profile from nanostructures

Hanwei Wang [a,b], Yun-Sheng Chen [a,c,d,e,*], Yang Zhao [a,b,d,f,*]

[a] Department of Electrical and Computer Engineering, University of Illinois Urbana-Champaign, Urbana, IL, USA
[b] Micro and Nanotechnology Laboratory, University of Illinois Urbana-Champaign, Urbana, IL, USA
[c] Beckman Institute for Advanced Science and Technology, University of Illinois Urbana-Champaign, Urbana, IL, USA
[d] Department of Bioengineering, University of Illinois Urbana-Champaign, Urbana, IL, USA
[e] Carle Illinois College of Medicine, University of Illinois Urbana-Champaign, Urbana, IL, USA
[f] Carl R. Woese Institute for Genomic Biology, University of Illinois Urbana-Champaign, Urbana, IL, USA

ARTICLE INFO

ABSTRACT

Understanding the mechanism of photoacoustic generation at the nanoscale is key to developing more efficient photoacoustic devices and agents. Unlike the far-field photoacoustic effect that has been well employed in imaging, the near-field profile leads to a complex wave-tissue interaction but is understudied. Here we show that the spatiotemporal profile of the near-field photoacoustic waves can be shaped by laser pulses, anisotropy, and the spatial arrangement of nanostructure(s). Using a gold nanorod as an example, we discovered that the near-field photoacoustic amplitude in the short axis is ~75 % stronger than the long axis, and the anisotropic spatial distribution converges to an isotropic spherical wave at ~50 nm away from the nanorod's surface. We further extend the model to asymmetric gold nanostructures by arranging isotropic nanoparticles anisotropically with broken symmetry to achieve a precisely controlled near-field photoacoustic "focus" largely within an acoustic wavelength.

1. Introduction

The photoacoustic effect, since discovered by Alexander Bell in 1880 [1], has wide applications in spectroscopy [2–4], medical imaging [5–10], and recently neuroscience [11]. The photoacoustic effect generates acoustic waves in an optically absorbing sample. Plasmonic nanostructures, including fabricated gold nanostructures [12] and synthetic nanoparticles [13–15], are popular photoacoustic materials [16], because they are chemically inert, have low toxicity, and, critically, their optical properties can be conveniently controlled by their geometries [17]. The plasmonic resonances of some anisotropic gold nanoparticles are located in the near-infrared (NIR) spectral region, also known as the tissue window, where light can penetrate deeper into tissue because of the minimum endogenous tissue absorption and scattering [18]. Due to their excellent optical properties and biocompatibility, these NIR gold nanoparticles play a critical role in developing theranostic agents [8,19, 20], photothermal therapy [21–23], neuron stimulation [11,24,25], and photoacoustic molecular imaging technologies [16,18,26].

Driven by the great interest in gold nanoparticles in photoacoustic applications [11,18,24,27–34], the fundamental mechanism of photoacoustic generation from various gold nanoparticles has been investigated theoretically and experimentally [18,35–38]. The photoacoustic generation in gold nanoparticle solutions is distinct from the photoacoustic generation in pure light-absorbing solid or liquid. In pure bulk materials, heat is confined within the same medium because of the optical homogeneity. On the other hand, in gold nanoparticles, during the photoacoustic process, the photon energy converts into heat, resulting in thermal expansion and relaxation. Because of the high thermal conductivity of gold and the nanoscopic size, the generated heat may leak out of the nanoparticles during light exposure, and a significant portion of the thermal energy can be deposited to the surrounding media (usually water or tissue), inducing photoacoustic waves from the surrounding media [36,38,39]. Compared to the bulk materials, the difference in confinement at the nanoscale leads to several unique photoacoustic properties. For example, different coating of the nanoparticles can affect the photoacoustic intensity [26,36,38,40–42], albeit with the same optical absorption. The size and shape of the nanoparticles affect the heat distribution, which can influence the photoacoustic conversion

* Corresponding authors at: Department of Electrical and Computer Engineering, University of Illinois Urbana-Champaign, Urbana, IL, USA
E-mail addresses: yunsheng@illinois.edu (Y.-S. Chen), yzhaoui@illinois.edu (Y. Zhao).

efficiency, i.e., the efficiency of converting photon energy to acoustic pressure [18,35,43]. These properties have paved new design rules for producing nanoparticles with effective photoacoustic signal generation in the far-field.

Recently, there has been a growing interest in photoacoustic devices [44–47], which employ the photoacoustic near-field effect, dramatically different from the far-field effect that is commonly used in photoacoustic imaging. Others and our previous work have shown that gold nanoparticle aggregation causes a nonlinear effect [48,49], which results in an enhancement of the photoacoustic fields and waves, suggesting that the nanoparticle near-field photoacoustic interactions may contribute to this nonlinear effect. Several recent studies of the photoacoustic near-field have revealed that the near-field distribution around nanoparticles and microparticles differs from the far-field prediction [38] and may even have a spatial distribution depending on the shape of the particle [50]. However, the near-field spatiotemporal profiles remain largely understudied for anisotropic nanoparticles and nanostructures within the spatial region much smaller than the wavelength of the associated acoustic pulse. This knowledge gap might be attributed to the fact that many existing studies record nanoparticle-generated photoacoustic signals with ultrasound transducers, where the near-field photoacoustic spatial profile was overlooked. However, the near-field photoacoustic profile is of paramount importance in the applications of cellular stimulation and photoacoustic induced drug release.

In this paper, we focus on analyzing the near-field photoacoustic profile of plasmonic nanostructures, and start with a gold nanorod as a representative anisotropic plasmonic nanostructure [51]. Our results show that the photoacoustic spatial profile is anisotropic within a spatial domain that is much smaller than the wavelength of the acoustic wave, yielding 74.6 % higher signal intensity along the transverse direction of the nanorod than in the longitudinal direction on the nanoparticle surface. This near-field spatial profile depends on the sizes and geometries of the nanostructure and the laser pulse durations. Further, we show that the near-field photoacoustic profile can be manipulated by the anisotropic spatial arrangement of isotropic gold nanostructures.

2. Results and Discussion

We use the following equation, $p(\mathbf{r}, t)$, to describe the photoacoustic spatiotemporal profile [52],

$$\left(\nabla^2 - \frac{1}{v_s^2} \frac{\partial}{\partial t^2} \right) p(\mathbf{r}, t) = -\frac{\beta}{\kappa v_s^2} \frac{\partial^2 T(\mathbf{r}, t)}{\partial t^2} \tag{1}$$

where v_s is the acoustic speed; β is the thermal expansion coefficient; κ is the isothermal compressibility, $\kappa = \frac{C_p}{\rho v_s^2 C_v}$; C_p is the heat capacity at constant pressure; and C_v is the heat capacity at constant volume. The acoustic speed v_s, the thermal expansion coefficient β, and the isothermal compressibility κ are distributed parameters of gold and water according to the spatial coordinate. Explicitly, the ratio between C_p and C_v is taken as 1 for both gold and water. The nanostructure (gold) parameters are $v_s = 3240 m/s$, $\beta = 14 \times 10^{-6} K^{-1}$, and $\rho = 19.3 \times 10^3 \ kg \ m^{-3}$. The medium (water) parameters are $v_s = 1481 m/s$, $\beta = 210 \times 10^{-6} K^{-1}$, and $\rho = 997 \ kg \ m^{-3}$. We assume a non-thermally resistive and non-lossy boundary condition for the nanostructures, i.e., the temperature is continuous, and the heat flux is conserved at the boundary. The thermal resistive boundary condition between nanostructure and media is discussed in Supplementary Note 1.

We use a semi-analytical approach to analyze the near-field photoacoustic profile. The detailed three-dimensional thermal profile governs the near-field photoacoustic generation; therefore, it requires numerical calculations. However, the comparison with far-field photoacoustic signals requires an extensive computational burden. To reduce the computational burden, we combine numerical calculations and analytical approaches in the following.

We first numerically calculate the time-dependent thermal distribution of a domain containing the gold nanorod and its surrounding media. We choose to start with a gold nanorod because it has been widely used in far-field photoacoustic research [18,26,36,49], is the simplest anisotropic nanostructure, and serves as a convenient model system. With a gold nanorod of 160 nm in length, 30 nm in width (i.e., an aspect ratio of 5.33), and water as the media, the absorption peak of the longitudinal mode of the nanorod falls in the second near-infrared (NIR-II) window (Fig. 1a). We simulate the nanorod absorption spectrum with a finite element solver (COMSOL Multiphysics 5.5, RF Module, Frequency Domain). The time-dependent intensity I of the laser pulse is modeled with a Gaussian function, $I = I_0 \cdot \exp\left(-\frac{1}{2} \frac{(t-t_0)^2}{\sigma^2} \right)$, where I_0 is the peak intensity, $I_0 = \frac{F}{\sqrt{2\pi}\sigma}$; F is the fluence of the laser; σ is the variance $\sigma = \frac{w}{2\sqrt{2 \ln 2}}$; w is the full-width-at-half-maximum (FWHM) of the laser pulse; t_0 is the center time of the pulse.

To begin with, we assume the laser fluence and pulse width to be 1 mJ cm^{-2} and 0.1 ns, respectively; the fluence is kept constant throughout the paper, and the pulse width is considered a variable in our later analysis. The laser pulse width is associated with the thermal confinement of the nanorod. If the pulse width is much shorter than the thermal relaxation time of the nanorod, the photoacoustic process is thermally confined; otherwise, the photoacoustic process is not thermally confined, where the heat transfer to the immediate media of the nanorod competes with the photothermal heating process. The thermal relaxation time of the nanorod, τ_t, defined as the time required to dissipate $1 - e^{-1}$ of the thermal energy with an impulse laser input [53]. We numerically simulate the thermal relaxation process with COMSOL Multiphysics 5.5 using the time domain heat transfer module. The thermal relaxation time is simulated to be 0.248 ns (Supplementary Note 2), which falls in the measured range of 0.1–0.4 ns for gold nanoparticles with a similar size [54]. The non-uniformity of the optical field due to the scattering of the nanostructure is insignificant at the nanoscale [55]; therefore, light will provide a close-to-homogeneous thermal excitation to the nanostructure, and we treat the absorption power density to be uniform within the nanostructure. If the process is thermally confined, the heat transfer between the nanorod and its media is negligible, and the second derivative of temperature in Eq. (1) can be simplified as

$$\frac{\partial^2 T}{\partial t^2} = \frac{1}{C_{nr} m_{nr}} \frac{\partial H}{\partial t} \tag{2}$$

where C_{nr}, m_{nr}, and H are the heat capacity, mass, and the total absorption power of the nanorod. Explicitly, the parameters are $C_m = 129 J kg^{-1} K^{-1}$ and $m_{nr} = 2.05 \times 10^{-18} kg$. $H = \sigma_{abs} I$, where σ_{abs} is the absorption cross-section of the nanorod. The time derivative of the laser's intensity is $\frac{\partial I}{\partial t} = -\frac{(t-t_0)}{\sigma^2} I_0 \cdot \exp\left(-\frac{1}{2} \frac{(t-t_0)^2}{\sigma^2} \right)$. If the process is not thermally confined, one can simulate the temperature distribution. Because of the large range of laser pulse widths being studied, we do not assume thermal confinement throughout our discussion.

The assumed laser pulse width of 0.1 ns is smaller but comparable to the thermal relaxation time, therefore, the time-dependent heat transfer cannot be ignored. As shown in Fig. 1, the numerical simulation considering the heating and cooling processes results in a lower second derivative of the nanorod's temperature, T'', than the analytical calculation (Eq. 2) by assuming thermal confinement (Fig. 1b). Fig. 1c shows the time evolution of the photoacoustic wave generated by the nanorod, which propagates through space with a far-field profile similar to a spherical wave but with a distinct anisotropic feature in the near-field.

The anisotropy of the near-field photoacoustic distribution is attributed to the nanorod's geometry and acoustic interference. Neglecting the acoustic scattering at the nanorod/water interface, we can calculate the photoacoustic field using Green's function in water $G(\mathbf{r}, t, \mathbf{r}', t') = \frac{\delta\left(t - t' - \frac{|\mathbf{r}-\mathbf{r}'|}{v_s} \right)}{4\pi|\mathbf{r}-\mathbf{r}'|}$. The photoacoustic pressure can be simplified as

a

b

c
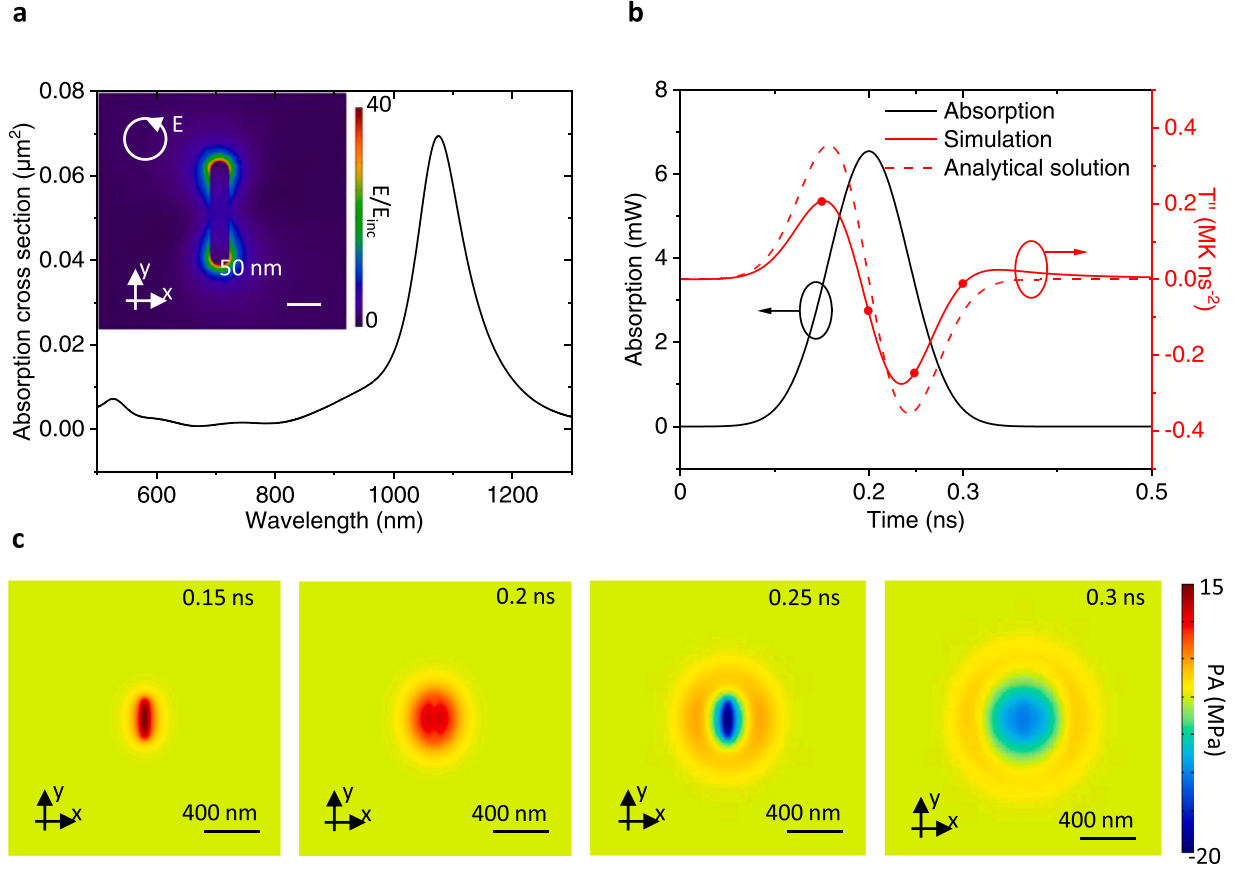
Fig. 1. | Calculated anisotropic photoacoustic near-field spatial distribution generated by a gold nanorod. **a**, Optical absorption spectrum. The nanorod has a length of 160 nm and a width of 30 nm. The laser has a fluence of 1 mJ cm^{-2} and a wavelength of 1100 nm. The laser is circularly polarized to excite both the longitudinal and transverse modes of the nanorod. Note that the particular handedness (left or right) is not critical regarding the nanorod's absorption. The inset shows the electric field distribution on resonance (at 1100 nm). The absorption spectrum and the electric field distribution are simulated with a finite element solver (COMSOL Multiphysics 5.5, RF Module, Frequency domain). **b**, Absorption and second derivative of temperature as a function of time. The temperature profile is simulated using a finite element solver (COMSOL Heat Transfer Module). **c**, Numerical simulation of the photoacoustic (PA) pressure wave using the partial differential Eq. (1), simulated with a finite element solver (COMSOL, PDE Module). The corresponding time frames are marked as the red dots in b.

$$p(\mathbf{r},t) = \frac{\beta}{4\pi\kappa v_s^2} \int d\mathbf{r}' \frac{1}{|\mathbf{r}-\mathbf{r}'|} \left. \frac{\partial^2 T(\mathbf{r}',t')}{\partial t'^2} \right|_{t'=t-\frac{|\mathbf{r}-\mathbf{r}'|}{v_s}} \tag{3}$$

When the photoacoustic source region (the nanorod and its immediate media) is comparably small to their distance to the measurement point (i.e., far-field), $|\mathbf{r}'| \ll |\mathbf{r}|$, the term $\frac{1}{|\mathbf{r}-\mathbf{r}'|} \approx \frac{1}{|\mathbf{r}|}$. On the other hand, when the laser pulse width is relatively long, the time shift of the photoacoustic wave generated from different parts of the source region is negligible, $\frac{|\mathbf{r}-\mathbf{r}'|}{v_s} \ll t$, thus, $t' \approx t$. With these two approximations, the photoacoustic distribution can be further simplified into a spherical wave:

$$p_{sph}\left(\mathbf{r},t\right) = \frac{\beta}{4\pi\kappa v_s^2} \frac{1}{|\mathbf{r}|} \int d\mathbf{r}' \frac{\partial^2 T(\mathbf{r}',t)}{\partial t'^2} \tag{4}$$

However, the spherical wave assumption fails to hold in the near-field. And when the pulse width is relatively short, the time-shift of the photoacoustic wave generated from different parts of the source region becomes significant; the positive acoustic pressure generated by one part may destructively interfere with a negative acoustic pressure caused by another. Both effects will lead to differences in the photoacoustic field distribution compared to the spherical wave described by 7(7).

As seen in Fig. 1c, the generated photoacoustic signal oscillates in time. To further analyze the spatial distribution of the photoacoustic near-field, we define the photoacoustic amplitude as the difference between the maximum and the minimum of the photoacoustic pressure over time, $P(\mathbf{r}) = \max(p(\mathbf{r},t),t) - \min(p(\mathbf{r},t),t)$. Note that the temporal profile of the photoacoustic pressure is asymmetrical under thermal non-confinement, so $\max(p(\mathbf{r},t),t) - \min(p(\mathbf{r},t),t) \neq 2\max(p(\mathbf{r},t),t)$. Fig. 2a shows the 2D photoacoustic amplitude distribution $P(\mathbf{r})$, calculated with Eq. (3). For comparison, Fig. 2b shows the photoacoustic amplitude distribution of a spherical wave $P_{sph}(\mathbf{r})$ given by 7(7). Although Eq. (3) and 7(7) are general to both thermal confined and non-confined scenarios, in the short pulse case, we use the Green's function together with the thermal confinement approximation (Eq. (2)) to reduce the computational burden.

The anisotropic spatial distribution in Fig. 2a motivates us to analyze the photoacoustic amplitude profiles along the transverse (x, or T) and longitudinal (y, or L) directions of the nanorod. With 0.1 ns laser pulse excitation, the pulse propagation length (Λ) defined as the FWHM pulse width multiplied by the acoustic speed $\Lambda = wv_s$ is 148 nm in water. This length scale is comparable to the length scale of the nanorod (160 nm); therefore, we anticipate discrepancies between the simulated photoacoustic amplitudes and the spherical wave estimated photoacoustic amplitude. Fig. 2c compares the simulated photoacoustic amplitudes along transverse and longitudinal directions with the semi-analytical solutions given by Eq. (3) and 7(7). The simulated photoacoustic amplitude deviates strongly from the far-field spherical wave estimation (7(7)) when the distance to the nanorod surface is less than 50 nm, approximately 1/3 of the pulse propagation length Λ. This distance can be considered as the near-field regime where the far-field approximation breaks down, suggested by the convergence of all solutions in Fig. 2c to
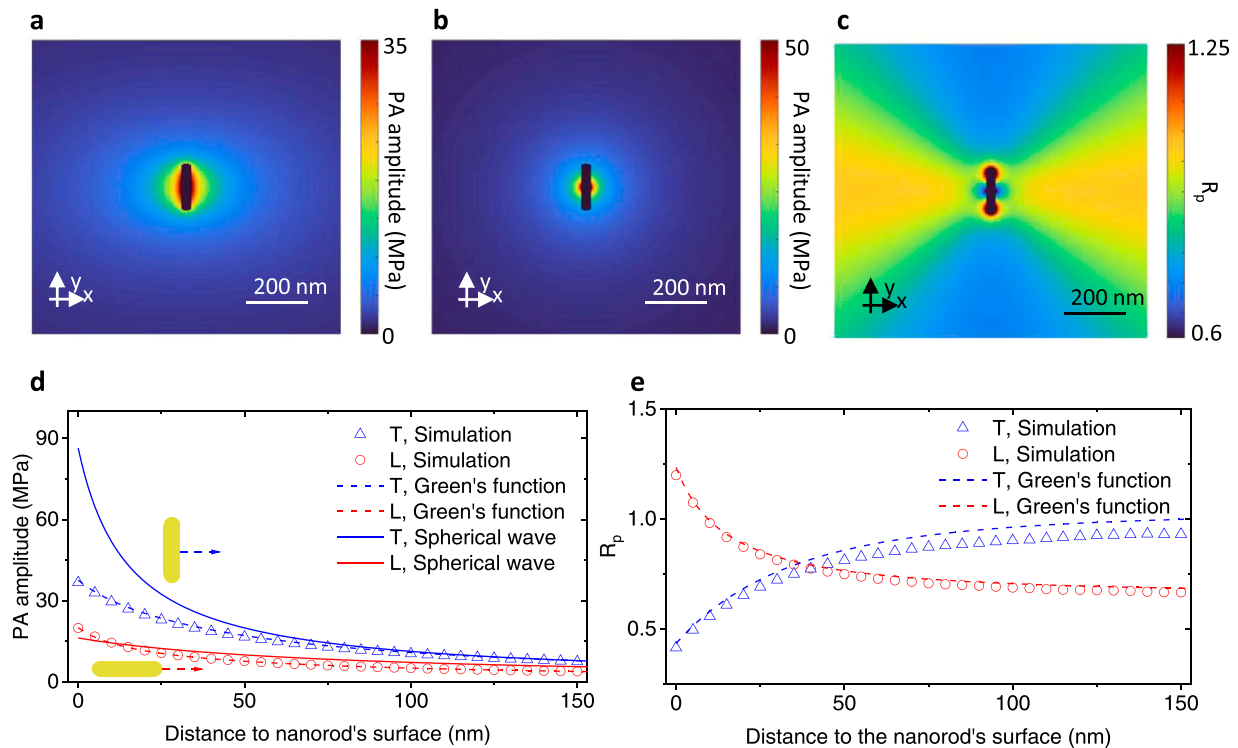
Fig. 2. | Influence of nanoparticle orientation on the near-field photoacoustic amplitude. a, The near-field photoacoustic (PA) amplitude of a nanorod calculated by the Green's function method. The field inside the nanorod is set as zero. b, The photoacoustic amplitude of a spherical wave given by 7(7). The source of the spherical wave locates at the center of the nanorod. c, Photoacoustic amplitude calculated using Multiphysics numerical simulation, the Green's function method (Eq. (3)), and spherical wave approximation (7(7)) along the transverse (T) and longitudinal (L) directions of the nanorod. The distance starts from the surface of the nanorod, as illustrated in the insets. d, 2D map of the correction coefficient R_p, which is the ratio between the photoacoustic amplitude in a to the spherical wave in b. e, R_p along the transverse (T) and longitudinal (L) directions, calculated using the numerical simulation and the Green's function method, showing good agreement in the near-field region.

the spherical wave estimation beyond this distance. Fig. 2c also demonstrates that the simulated results and the Green's function method match well even within the near-field. The difference between the numerical simulation and that from Green's function method is attributed to the leaked heat to the media. Due to the larger boundary area along the transverse direction than the longitudinal direction, the difference contributed by such approximation is larger along the transverse direction. Nevertheless, the influence of this effect is minor, which has a difference smaller than 5 % for 0.1 ns laser pulses and is expected to be even smaller for longer pulses, suggesting that the Green's function method can serve as a good approximation in the near-field regime.

To elaborate on the anisotropic near-field property of the nanorod, we define a unitless correction coefficient R_p, which is the ratio of the photoacoustic near-field amplitude to the photoacoustic amplitude estimated from the spherical wave:

$$R_p(\mathbf{r}) = \frac{P(\mathbf{r})}{P_{sph}(\mathbf{r})} \qquad (5)$$

Fig. 2d shows the 2D distribution of R_p given by the ratio of Fig. 2a and Fig. 2b, highlighting the spatial anisotropy of the photoacoustic amplitude along the transverse and longitudinal directions. In contrast, the photoacoustic near-field for isotropic nanostructures is similar to a spherical wave and the R_p coefficient is close to 1 (Supplementary Note 3). Fig. 2e analyzes how R_p varies as a function of the distance away from the nanorod's surface along both directions, quantifying the differences between the near-field photoacoustic amplitude $P(\mathbf{r})$ and the amplitude estimated with spherical waves $P_{sph}(\mathbf{r})$ and, thus, the anisotropy. On the nanorod surface, $P(\mathbf{r})$ is 20.0 % higher than $P_{sph}(\mathbf{r})$ along the longitudinal direction but 58.5 % lower along the transverse direction. It is worth noting that the absolute value of photoacoustic amplitude at the

transverse location remains higher than at the longitudinal location because |**r**| is smaller at the width than the length of the nanorod and **r**'s origin is the nanorod center. As a result, the photoacoustic amplitude in the transverse direction is 74.6 % higher than the longitudinal direction on the nanorod surface. This is because there are more thermal sources contributing to the transverse direction than the longitudinal direction, which should not be confused with the electromagnetic field distribution shown in the inset of Fig. 1a.

The near-field photoacoustic amplitude can be further controlled by laser pulse widths due to heat transfer and acoustic interference. To fairly compare across different pulse widths, we use normalized thermal energy $Q''w^2$. Q'' is the second derivative of the nanorod's thermal energy, where Q is calculated by $Q = \rho C_{nr} \int_{nr} T dV$ and w is the laser pulse width. $Q''w^2$ is proportional to the normalized photoacoustic pressure (see more details in Supplementary Note 4). Fig. 3a shows the comparisons of normalized thermal energy across different pulse widths; the N-shaped analytical solution is calculated as the time derivative of the absorbed power of the nanorod according to Eq. (2) under the thermal confinement condition. Therefore, the analytical solution shows the highest value. The normalized thermal energy is higher with shorter pulse durations, which matches our expectations that the photoacoustic amplitude increases (Fig. S3c) as the laser pulse duration decreases because less thermal energy is leaked out to the surrounding medium, and it is approaching the analytical solution condition.

We conducted a frequency analysis of the photoacoustic pulses to investigate how the laser pulse width changes the frequency responses of the photoacoustic signals. It is known that the photoacoustic pulses generated from nanoparticles contain a broad band of frequencies. The photoacoustic central frequency is tunable from several MHz to hundreds of GHz for laser pulses ranging from 0.01 ns to 100 ns
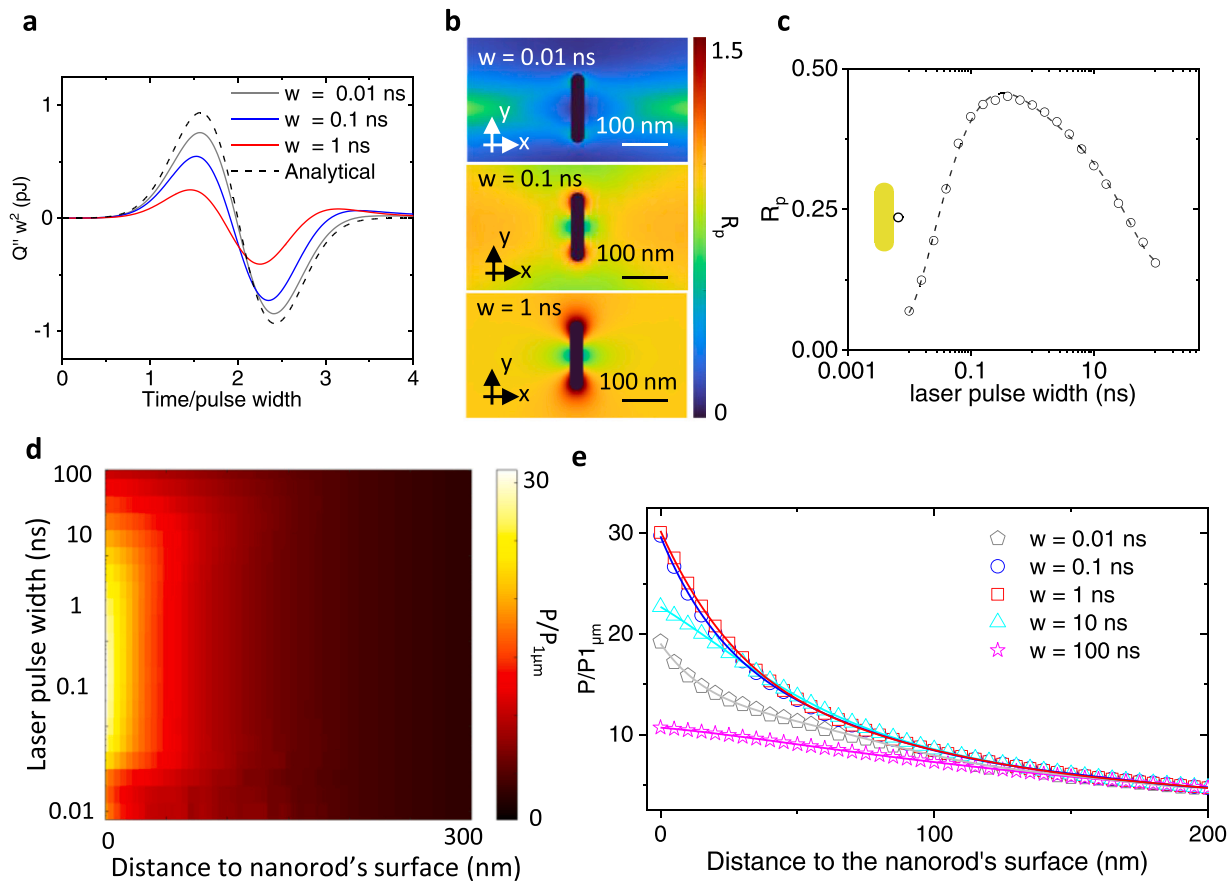
Fig. 3. | Tuning the near-field photoacoustic amplitude and decay rate with laser pulse widths. a, The second time derivative of the nanorod's thermal energy Q versus time with different pulse widths. The thermal energy is normalized by multiplying the square of the pulse width (Supplementary Note 4), and the time is normalized by dividing the pulse width. b, 2D map of R_P with different pulse widths. c, R_P on the surface of the nanorod (with the position marked in the inset) as a function of the pulse width, calculated using the Green's function method. For pulse widths longer than 1 ns, the time shift due to the size of the nanorod can be neglected. d, The photoacoustic pressure (P) normalized by the far-field photoacoustic pressure at $\mathbf{r}_{ff} = 1$ μm (denoted as $P_{1\,\mu m}$) along the transverse direction as a function of the pulse width and the distance from the nanorod surface. e, Normalized photoacoustic pressure versus distance with different pulse widths showing the spatial decay rate.

(Supplementary Note 5). While the high-frequency components cannot propagate to the far-field, within the near-field regime, the duration of the laser pulse is a convenient approach to tune the frequency responses.

We discovered the different laser pulse widths also affect the near-field photoacoustic decay rate over distance. Note that here the decay rate is the initial photoacoustic amplitude distribution near a nanorod caused by thermal distribution, not the decay caused by the water attenuation of the propagating photoacoustic wave. According to Eqs. (4) and (5), the distribution of the photoacoustic amplitude can be written as:

$$P(\mathbf{r}) = \frac{R_p(\mathbf{r})A_0}{|\mathbf{r}|} \qquad (6)$$

where A_0 is the source intensity defined as $A_0 = \max(A(t),t) - \min(A(t),t)$, and $A(t) = \frac{\beta}{4\pi\kappa v_s^2} \int d\mathbf{r}' \frac{\partial^2 T(\mathbf{r}',t)}{\partial t'^2}$.

Since the photoacoustic amplitude will converge to the spherical wave (7(7)) at a distance much larger than 50 nm, R_p will approach 1 in the far-field for longer pulses ($w > 1$ ns). Based on Eq. (6), the near-field photoacoustic amplitude can be written as $P_{nf} = R_p(\mathbf{r_t})\frac{|\mathbf{r}_{ff}|}{|\mathbf{r}_{nf}|}P_{ff}$, where P_{ff} and P_{nf} are the far-field and near-field photoacoustic amplitude, $\mathbf{r}_{nf}$ and $\mathbf{r}_{ff}$ are the near-field and far-field displacements with respect to the nanorod's center, and R_p is evaluated in the near-field at the point of interest. R_p reflects how fast the photoacoustic near-field decays. A higher R_p with a certain far-field amplitude represents a higher near-

field photoacoustic amplitude at the point of interest, in other words, a more rapidly decayed near-field in distance. By comparing R_p in Fig. 3c and its spatial distribution in Fig. 3b, one can see that R_p reaches its peak value with a pulse width between 0.1 ns and 1 ns.

When the pulse width is relatively short and the pulse propagation length Λ is smaller than the nanorod's size, the positive and negative peaks of the photoacoustic wave generated by different parts of the source region destructively interfere with each other in the near-field, which will affect the near-field photoacoustic amplitude and change the photoacoustic pulse shape in the time domain (Fig. S4a, Supplementary Note 5). On the other hand, when the pulse width is longer than the thermal relaxation time, the heat transfer becomes significant, and the photoacoustic amplitude decreases as the pulse width increases. As both effects affect the near-field photoacoustic amplitude, our estimated R_p using the Green's function method confirms a peak R_p at the pulse width near the thermal relaxation time-scale and decreases toward longer and shorter pulse durations (Fig. 3c). Scrutinizing Fig. 3c suggests that to reach over 70 % of the peak R_p, the laser should have a pulse propagation length longer than 0.46 of the nanorod's length, i.e.,

$$v_s \cdot w > 0.46 \cdot l \qquad (7)$$

and a pulse width shorter than 42.13 of the thermal relaxation time, i.e.,

$$w < 42.13 \cdot \tau_t \qquad (8)$$

To compare the spatial decay rate more intuitively, we fix the far-

field photoacoustic amplitude at 1 μm and calculate the near-field with different pulse widths (Fig. 3d). Fig. 3e shows the photoacoustic near-field decays with a faster rate over distance for pulse widths of 0.1 ns and 1 ns than the other pulse widths, corroborating the optimal range of laser pulse widths for fast decayed photoacoustic near-field in Fig. 3c.

To optimize photoacoustic signals, many existing works have discussed the influence of physical dimensions and coating on the far-field photoacoustic signals [18,26,35–37]. Similarly, the physical dimensions and coating also affect the near-field photoacoustic amplitude. Both the photoacoustic equation (Eq. (1)) and the heat transfer equation (Supplementary Eq. (S6)) can be scaled up or down of its dependent variables without changing the correction coefficient R_p. 10(10) and 11(11) remain valid regardless of the nanorod's size (Supplementary Note 6). We define a scaling factor, a, as the ratio of the nanorod's length to 160 nm (i.e., our initial nanorod length). When the nanorod is rescaled by a factor a, equivalently, the spatial variable is rescaled by $1/a$, and the temporal domain is rescaled by a. In this way, the heat transfer equation remains the same for different sizes of the nanorod so that one can optimize the nanorod dimensions while maintaining the nanorod's aspect ratio and, thus, the optical resonance. During the photoacoustic generation, optical absorption efficiency and heat transfer will be affected by the nanorod dimension. Considering both effects, there is an optimal nanorod dimension for generating photoacoustic near-field amplitude at a given laser pulse width (Fig. S5, Supplementary Note 6).

In general, a smaller nanorod yields a higher absorption power density (Fig. S3b) but also a faster heat transfer and, consequently, a stronger cooling effect from the medium (Supplementary Note 6). Considering both effects, there is an optimal nanorod dimension for generating photoacoustic near-field amplitude at a given laser pulse width (Fig. 4). We observed that the optimal nanorod size is dependent on the laser pulse width and is approximately linear to the logarithm of the pulse width. Through linear fitting of the optimal scaling factor a, with the logarithm of the laser pulse width w (Fig. S3d), the optimal scaling factor is approximately

$$a_{opt} = c_1 + c_2 \cdot \log(w/1ns) \tag{9}$$

where the two coefficients are $c_1 = 0.0591$ and $c_2 = 0.402$. For example, for laser pulse widths of 0.1 ns, 1 ns, and 10 ns, the optimal nanorod length is around 50 nm, 65 nm, and 80 nm (Fig. S3c), respectively. The photoacoustic amplitude is enhanced by 64.91 %, 56.56 %, and 48.36 % accordingly compared to the nanorod with a length of 160 nm. Note that this is the near-field photoacoustic amplitude generated by a single nanorod with the assumption of a fixed laser fluence, distinct from that generated from an ensemble of nanoparticles in solution.

The near-field photoacoustic signal can be further enhanced with a coating, such as lipid [38,42,56], because the coating layer changes interfacial thermal resistance and the nanorod becomes more thermally confined at the same physical length. However, a thicker coating also increases the distances between the nanorod and the coating surface, which decreases the photoacoustic amplitude on the coating surface; therefore, there is an optimal coating thickness as well (Supplementary Note 6).

The overall optimal nanorod design and laser pulse width are shown in Fig. 4 to maximize the near-field photoacoustic amplitude by considering both the nanorod size and lipid coating thickness. Specifically, the shaded region between the black and red curves offers a rapidly decayed photoacoustic field, where R_p is over 70 % of its peak value. The relationship between the laser pulse width and the nanorod's size for the optimal photoacoustic amplitude is the blue curve (given by 12(12)). The scaling factor should be between 0.2 and 0.47, corresponding to a nanorod's length of 32–75.2 nm with a resonance in NIR II, and the laser pulse width should be between 0.01 ns and 4.6 ns according to these dimensions. The optimal thickness of a lipid coating should be between 8.5 nm and 25.6 nm, given by Eq. (S10), shown as the cyan curve in Fig. 4.

This abovementioned optimization methodology is not limited to gold nanorods but can be applied to near-field photoacoustic amplitude generated by general nanostructures. For example, the anisotropic near-field distribution can also be formed by isotropic gold nanospheres in an anisotropic arrangement. We discovered that a similar anisotropic photoacoustic near-field distribution, as shown in Fig. 1, can be formed using a linear array of three isotropic gold nanospheres (Fig. S7, Supplementary Note 7). The field distribution and the decay rate highly depend on the arrangement of the nanostructure. The near-field anisotropy can be further manipulated by breaking the symmetry of the arrangement. As shown in Fig. 5a, when the top and bottom nanospheres are displaced by 30 nm toward the +x direction, the near-field photoacoustic pressure on the right side of the nanospheres becomes stronger than the left (Fig. 5b). The stronger photoacoustic amplitude at a certain location can be further enhanced by introducing more asymmetry in the nanostructure (Fig. 5c and 5d) and optimized. Here, we assume the same absorption power density as the nanorod at 1100 nm in Fig. 1a. Due to the spatiotemporal linearity of the photoacoustic equation (Eq. (1)), the absorption-normalized photoacoustic near-field distribution is uniquely determined by the nanostructure's geometry and the laser pulse width and independent of the laser's polarization and propagation direction.

The photoacoustic signal generated at the nanostructures will decay with the distance. The spatial distribution and decay rate of this signal can be precisely controlled by the nanostructure arrangement. Fig. 5 creates a near-field signal that is asymmetric due to the anisotropic nanostructures; the decay of the near-field photoacoustic intensity on the right side of the nanostructure is slower than that from the left side of the nanostructure. Spatially, this is analogous to a "focusing" hot spot in the photoacoustic signal if there is a threshold intensity. Through further optimization, the "focal point" with an intensity stronger than the threshold can be precisely controlled.

In summary, we develop a systematic analysis of the near-field
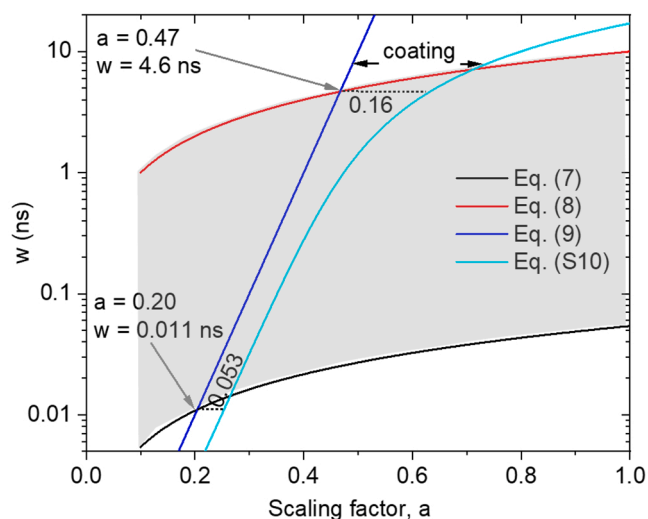
Fig. 4. | Design criteria of the laser pulse widths, nanorod materials and dimensions for optimizing near-field photoacoustic amplitude. The black, red, blue and cyan curves are given by conditions in 10(10), 11(11), 12(12), and Eq. (S10), respectively. The shaded region between the black and red curves provides the highest decay rate of the photoacoustic field, and the blue curve provides the highest photoacoustic intensity. The blue curve between the two arrows marks the optimal condition considering both the decay rate and the photoacoustic intensity. The distance along x direction between the blue and the cyan curves shows the optimal coating thickness of a lipid shell. The shaded region illustrates the more rapidly decayed photoacoustic near-field, yielding R_p over 70 % of its peak value. w denotes the laser pulse width; a denotes the scaling factor of the nanorod.
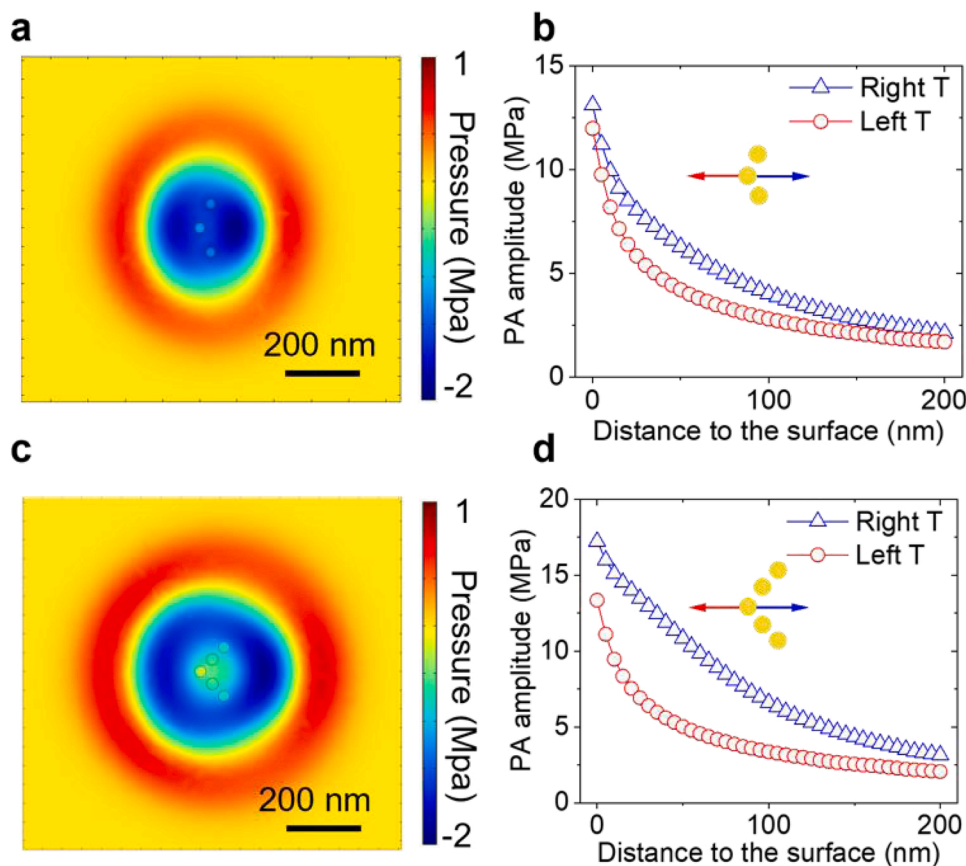
Fig. 5. | Manipulating the near-field photoacoustic distribution using anisotropic nanostructures. a, Simulated photoacoustic (PA) amplitude at 0.35 ns generated by three nanospheres. The top and bottom spheres are displaced by 30 nm compared to the case in Fig. S3. The nanospheres have a radius of 15 nm and a separation of 65 nm. The laser pulse width is 0.1 ns. We use the same absorption power density as the nanorod at 1100 nm in Fig. 1a. b, Simulated PA amplitude along the transverse (T) direction. Blue curve shows the PA amplitude to the right of the nanostructure; the red curve shows the PA amplitude to the left of the nanostructure. c, Simulated PA amplitude at 0.35 ns generated by five nanospheres. The nanospheres have 25 nm separations in the y direction and 30 nm separation in the x direction, showing a strong anisotropy in the near-field PA spatial distribution. d, Simulated PA amplitude along the left and right transverse (T) directions for the five nanospheres case.

photoacoustic profile in this paper, starting from a representative anisotropic gold nanoparticle. The laser pulse width is a tunable parameter to control the decay rate of the photoacoustic near-field. One can consider the near-field photoacoustic spatial distribution as the spatial 'resolution' of the nanostructure, where such a near-field photoacoustic signal extends beyond the nanostructure region and interacts with their immediate medium. Our results show that the near-field photoacoustic amplitude at a specific location can be optimized. The destructive acoustic interference reduces the near-field photoacoustic amplitude for short laser pulses, and thermal non-confinement reduces the photoacoustic amplitude for long laser pulses; therefore, for specific dimensions of the nanostructure, there is an optimal laser pulse duration. Our study provides a general design rule for choosing the laser pulses, optimizing the sizes, and designing the anisotropy of a nanostructure to manipulate and achieve a designated near-field photoacoustic distribution for enhancing localized interactions.

CRediT authorship contribution statement

Y.-S.C. and Y.Z. conceived the idea. H.W. conducted the theoretical studies and numerical simulations. All authors contributed to the analysis of the data and writing of the manuscript.

Declaration of Competing Interest

The authors declare that they have no known competing financial interests or personal relationships that could have appeared to influence the work reported in this paper.

Data Availability

Data will be made available upon request. The datasets generated

during and/or analyzed during the current study are available from the corresponding authors upon reasonable request.

Appendix A. Supporting information

Supplementary data associated with this article can be found in the online version at doi:10.1016/j.pacs.2022.100425.

References

[1] A.G. Bell, LXVIII. Upon the production of sound by radiant energy, Lond., Edinb., Dublin Philos. Mag. J. Sci. 11 (1881) 510–528.
[2] G.A. West, J.J. Barrett, D.R. Siebert, K.V. Reddy, Photoacoustic spectroscopy, Rev. Sci. Instrum. 54 (1983) 797–817.
[3] A. Miklos, P. Hess, Z. Bozoki, Application of acoustic resonators in photoacoustic trace gas analysis and metrology, Rev. Sci. Instrum. 72 (2001) 1937–1955.
[4] A.A. Kosterev, Y.A. Bakhirkin, R.F. Curl, F.K. Tittel, Quartz-enhanced photoacoustic spectroscopy, Opt. Lett. 27 (2002) 1902–1904.
[5] A.B.E. Attia, et al., A review of clinical photoacoustic imaging: current and future trends, Photoacoustics 16 (2019), 100144.
[6] L.H.V. Wang, S. Hu, Photoacoustic tomography: in vivo imaging from organelles to organs, Science 335 (2012) 1458–1462.
[7] A. De La Zerda, et al., Carbon nanotubes as photoacoustic molecular imaging agents in living mice, Nat. Nanotechnol. 3 (2008) 557–562.
[8] Y.J. Liu, P. Bhattarai, Z.F. Dai, X.Y. Chen, Photothermal therapy and photoacoustic imaging via nanotheranostics in fighting cancer, Chem. Soc. Rev. 48 (2019) 2053–2108.
[9] V. Ntziachristos, Going deeper than microscopy: the optical imaging frontier in biology, Nat. Methods 7 (2010) 603–614.

[10] S.Y. Emelianov, P.-C. Li, M. O'Donnell, Photoacoustics for molecular imaging and therapy, Phys. Today 62 (2009) 34.

[11] Y. Jiang, et al., Neural Stimulation in vitro and in vivo by photoacoustic nanotransducers, Matter 4 (2021) 654–674.

[12] H. Wang, D.W. Brandl, P. Nordlander, N.J. Halas, Plasmonic nanostructures: artificial molecules, Acc. Chem. Res. 40 (2007) 53–62.

[13] S.E. Lohse, C.J. Murphy, The quest for shape control: a history of gold nanorod synthesis, Chem. Mater. 25 (2013) 1250–1261.

[14] K.L. Kelly, E. Coronado, L.L. Zhao, G.C. Schatz, The optical properties of metal nanoparticles: the influence of size, shape, and dielectric environment, J. Phys. Chem. B 107 (2003) 668–677.

[15] M.C. Daniel, D. Astruc, Gold nanoparticles: assembly, supramolecular chemistry, quantum-size-related properties, and applications toward biology, catalysis, and nanotechnology, Chem. Rev. 104 (2004) 293–346.

[16] J. Weber, P.C. Beard, S.E. Bohndiek, Contrast agents for molecular photoacoustic imaging, Nat. Methods 13 (2016) 639–650.

[17] M.-F. Tsai, et al., Au nanorod design as light-absorber in the first and second biological near-infrared windows for in vivo photothermal therapy, ACS Nano 7 (2013) 5330–5342.

[18] Y.-S. Chen, Y. Zhao, S.J. Yoon, S.S. Gambhir, S. Emelianov, Miniature gold nanorods for photoacoustic molecular imaging in the second near-infrared optical window, Nat. Nanotechnol. 14 (2019) 465–472.

[19] J. Guo, et al., Gold nanoparticles enlighten the future of cancer theranostics, Int. J. Nanomed. 12 (2017) 6131–6152.

[20] H.C. Huang, S. Barua, G. Sharma, S.K. Dey, K. Rege, Inorganic nanoparticles for cancer imaging and therapy, J. Control. Release 155 (2011) 344–357.

[21] J.B. Vines, J.-H. Yoon, N.-E. Ryu, D.-J. Lim, H. Park, Gold nanoparticles for photothermal cancer therapy, Front. Chem. 7 (2019).

[22] M.R.K. Ali, Y. Wu, M.A. El-Sayed, Gold-nanoparticle-assisted plasmonic photothermal therapy advances toward clinical application, J. Phys. Chem. C 123 (2019) 15375–15393.

[23] J. Shah, et al., Photoacoustic imaging and temperature measurement for photothermal cancer therapy, J. Biomed. Opt. 13 (2008), 034024.

[24] S. Yoo, S. Hong, Y. Choi, J.-H. Park, Y. Nam, Photothermal inhibition of neural activity with near-infrared-sensitive nanotransducers, ACS Nano 8 (2014) 8040–8049.

[25] C. Paviolo, P.R. Stoddart, Gold nanoparticles for modulating neuronal behavior, Nanomaterials 7 (2017) 92.

[26] Y.-S. Chen, et al., Silica-coated gold nanorods as photoacoustic signal nanoamplifiers, Nano Lett. 11 (2011) 348–354.

[27] W. Li, X. Chen, Gold nanoparticles for photoacoustic imaging, Nanomedicine 10 (2015) 299–320.

[28] R. García-Álvarez, et al., Optimizing the geometry of photoacoustically active gold nanoparticles for biomedical imaging, ACS Photonics 7 (2020) 646–652.

[29] M.H. Xu, L.H.V. Wang, Photoacoustic imaging in biomedicine, Rev. Sci. Instrum. 77 (2006).

[30] T. Kim, Q.Z. Zhang, J. Li, L.F. Zhang, J.V. Jokerst, A gold/silver hybrid nanoparticle for treatment and photoacoustic imaging of bacterial infection, Acs Nano 12 (2018) 5615–5625.

[31] S. Mallidi, et al., Multiwavelength photoacoustic imaging and plasmon resonance coupling of gold nanoparticles for selective detection of cancer, Nano Lett. 9 (2009) 2825–2831.

[32] K.H. Song, C. Kim, K. Maslov, L.V. Wang, Noninvasive in vivo spectroscopic nanorod-contrast photoacoustic mapping of sentinel lymph nodes, Eur. J. Radiol. 70 (2009) 227–231.

[33] J.L. Carvalho-de-Souza, et al., Photosensitivity of neurons enabled by cell-targeted gold nanoparticles, Neuron 86 (2015) 207–217.

[34] Y.-S. Chen, et al., Enhanced thermal stability of silica-coated gold nanorods for photoacoustic imaging and image-guided therapy, Opt. Express 18 (2010) 8867–8878.

[35] R. Garcia-Alvarez, et al., Optimizing the geometry of photoacoustically active gold nanoparticles for biomedical imaging, ACS Photonics 7 (2020) 646–652.

[36] Y.S. Chen, W. Frey, S. Aglyamov, S. Emelianov, Environment-dependent generation of photoacoustic waves from plasmonic nanoparticles, Small 8 (2012) 47–52.

[37] R. Gao, et al., Opto-acoustic effect of Au nanoparticles in water under irradiation of pulse laser, Optik 202 (2020), 163512.

[38] K. Shahbazi, W. Frey, Y.-S. Chen, S. Aglyamov, S. Emelianov, Photoacoustics of core–shell nanospheres using comprehensive modeling and analytical solution approach, Commun. Phys. 2 (2019) 1–11.

[39] G.A. Pang, F. Poisson, J. Laufer, C. Haisch, E. Bossy, Theoretical and experimental study of photoacoustic excitation of silica-coated gold nanospheres in water, J. Phys. Chem. C 124 (2020) 1088–1098.

[40] J.V. Jokerst, M. Thangaraj, P.J. Kempen, R. Sinclair, S.S. Gambhir, Photoacoustic imaging of mesenchymal stem cells in living mice via silica-coated gold nanorods, Acs Nano 6 (2012) 5920–5930.

[41] D.P. O'Neal, L.R. Hirsch, N.J. Halas, J.D. Payne, J.L. West, Photo-thermal tumor ablation in mice using near infrared-absorbing nanoparticles, Cancer Lett. 209 (2004) 171–176.

[42] J.H. Kang, Y.T. Ko, Lipid-coated gold nanocomposites for enhanced cancer therapy, Int. J. Nanomed. 10 (2015) 33.

[43] Y. Mantri, J.V. Jokerst, Engineering plasmonic nanoparticles for enhanced photoacoustic imaging, ACS nano 14 (2020) 9408–9422.

[44] Y. Jiang, et al., Optoacoustic brain stimulation at submillimeter spatial precision, Nat. Commun. 11 (2020).

[45] L.L. Shi, et al., Non-genetic photoacoustic stimulation of single neurons by a tapered fiber optoacoustic emitter, Light-Sci. Appl. 10 (2021).

[46] N. Zheng, et al., Photoacoustic carbon nanotubes embedded silk scaffolds for neural stimulation and regeneration, Acs Nano 16 (2022) 2292–2305.

[47] D.E. Green, J.P. Longtin, B. Sitharaman, The effect of nanoparticle-enhanced photoacoustic stimulation on multipotent marrow stromal cells, Acs Nano 3 (2009) 2065–2072.

[48] S.Y. Nam, L.M. Ricles, L.J. Suggs, S.Y. Emelianov, Nonlinear photoacoustic signal increase from endocytosis of gold nanoparticles, Opt. Lett. 37 (2012) 4708–4710.

[49] Y.-S. Chen, S.J. Yoon, W. Frey, M. Dockery, S. Emelianov, Dynamic contrast-enhanced photoacoustic imaging using photothermal stimuli-responsive composite nanomodulators, Nat. Commun. 8 (2017) 15782.

[50] Y. Li, H. Fang, C. Min, X. Yuan, Simulating photoacoustic waves produced by individual biological particles with spheroidal wave functions, Sci. Rep. 5 (2015) 1–11.

[51] C.J. Murphy, et al., Anisotropic metal nanoparticles: synthesis, assembly, and optical applications, J. Phys. Chem. B 109 (2005) 13857–13870.

[52] L.V. Wang, H.-i Wu, Biomedical Optics: Principles and Imaging, John Wiley & Sons, 2012.

[53] R. Yadav, Definitions in laser technology, J. Cutan. aesthetic Surg. 2 (2009) 45.

[54] M. Hu, G.V. Hartland, Heat dissipation for Au particles in aqueous solution: relaxation time versus size, J. Phys. Chem. B 106 (2002) 7029–7033.

[55] G.S. He, et al., Scattering and absorption cross-section spectral measurements of gold nanorods in water, J. Phys. Chem. C 114 (2010) 2853–2860.

[56] Y.-S. Chen, et al., Ultra-high-frequency radio-frequency acoustic molecular imaging with saline nanodroplets in living subjects, Nat. Nanotechnol. 16 (2021) 717–724.
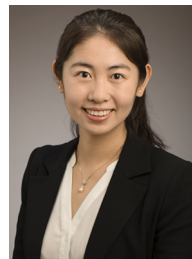
Yang Zhao is an assistant professor at the University of Illinois, Urbana-Champaign, Department of Electrical and Computer Engineering. She is affiliated with the Micro and Nanotechnology Laboratory and has a courtesy appointment with the Department of Bioengineering, and the Institute for Genomic Biology. Prof. Zhao received her Ph.D. in Electrical and Computer Engineering from the University of Texas at Austin, advised by Professor Andrea Alù. Following her Ph.D., she served as a postdoctoral research fellow in Materials Science at Stanford University, advised by Professor Jennifer A. Dionne. Prof. Zhao directs the BioNanophotonics lab at UIUC. Her research group is interested in studying nano-scale forces and fields by developing optical, nanophotonic, and photoacoustic tools, these tools are fundamental for imaging, sensing, and actuation across subwavelength to wavelength scales.